Proceedings of the 11th Brazilian Congress of Thermal Sciences and Engineering -- ENCIT 2006
Braz. Soc. of Mechanical Sciences and Engineering -- ABCM, Curitiba, Brazil,- Dec. 5-8, 2006

Paper CIT06-596

OPTIMAL DESIGN OF NON-NEWTONIAN, MICRO-SCALE VISCOUS PUMPS FOR BIOMEDICAL DEVICES – PRELIMINARY RESULTS

Alexandre K. da Silva
Department of Mechanical Engineering, University of Hawaii – Manoa, 2540 Dole St., Holmes Hall 302, Honolulu, HI 96822, USA
e-mail: akds@hawaii.edu

Marcelo H. Kobayashi
Department of Mechanical Engineering, University of Hawaii – Manoa, 2540 Dole St., Holmes Hall 302, Honolulu, HI 96822, USA
e-mail: marcelok@hawaii.edu

Carlos F. M. Coimbra
Department of Mechanical Engineering, University of Hawaii – Manoa, 2540 Dole St., Holmes Hall 302, Honolulu, HI 96822, USA
School of Engineering, University of California, P.O. Box 2039, Merced, CA 95344, USA
e-mail: coimbra@hawaii.edu

Abstract. *The present paper addresses the numerical optimization of geometrical parameters of non-Newtonian micro-scale viscous pumps for biomedical devices. The objective is to maximize the mass flow rate per unit of shaft power consumed by the rotor when an external pressure load is applied along the channel that houses the rotor. Two geometric parameters are considered in the optimization process: (i) the height of the channel that houses the rotor (H) and (ii), the eccentricity (ε) of the rotor. Three different micro scale viscous pump configurations were tested: a straight housed pump (I-shaped housing) and two curved housed pumps (L- and U-shaped housings). The stress-strain constitutive law is modeled by a power-law relation. The results show that the geometric optimization of micro scale viscous pumps is critical since the mass flow rate propelled by the rotor is highly dependent on ε and H. Numerical simulations indicate that mass flow rate is maximized when $\varepsilon \sim 0$, namely when the rotor is placed at a distance of 0.05 radii from the lower wall. The results also show that micro scale viscous pumps with curved housing provide higher mass flow rate per unit of shaft power consumed when compared with straight housed pumps. The results are presented in terms optimized dimensions of all three configurations (i.e., H_{opt} and ε_{opt}) and for values of the power-law index varying between 0.5 (shear thinning fluids) and 1.5 (shear-thickening fluids).*

Keywords*. Micro-Scale Viscous Pumps, Optimal Design, MEMS, Biomedical Pumps, Non-Newtonian Flow.*

1. Introduction

Advances in the miniaturization of electro mechanical systems have enabled the fabrication of microsystems or microelectromechanical systems (MEMS), which offer several advantages over conventional devices. These advantages include superior resolution, precision and sensitivity, lower costs, and reliability due to redundancy. In biological applications there is also the possibility of incorporating sensing, processing, and actuation nearby or on the same substrate – see the recent reviews on MEMS Judy (2001) and Ziaie *et al.* (2004). Because of their physical and engineering significance as well as the relevance of their applications, micropumps have figured prominently among the development of MEMS.

Micropumps, broadly defined as having dimensions smaller than 100 μm, have a myriad of applications ranging from micro total analysis systems (μTAS) Reyes *et al.* (2002), Verpoorte (2002) and Auroux *et al.* (2002), to mass spectrometer systems and micro propulsion in space exploration Micci and Ketsdever (2000). Micro total analysis systems or "lab on a chip", whose primary research works aim at biological and life sciences, is expanding rapidly. Indeed, labs on a chip have been successfully used, for instance, in the culture and handling of cells, DNA separation and analysis, DNA sequencing, chiral separation of amino acids, antibody analysis, determination of active ingredients in a drug, determination of the presence of explosive compounds and polymerase chain reaction – see the reviews Reyes *et al.* (2002) and Verpoorte (2002). Common to all these devices is the need to pump fluid at flow rates of up to 1000 milliliter per minute through dimensions of the micro or nano scales.

Contrary to microelectronics, that succeeded in scaling down its transistors and systems to provide faster and cheaper devices, pumping does not, as a rule, benefit from miniaturization. Actually, ordinary inertia based devices, such as centrifugal pumps, do not work at the very low Reynolds number commonly associated with the micropumping requirements. Instead, effective micropumps have fallen in one of the following two main categories: the positive-displacement or reciprocating pumps and the dynamic or continuous flow pumps – see the recent reviews Nguyen (2002), Laser and Santiago (2004) and Woias (2004).

Typically, reciprocating micropumps use pulsating surface motion to displace the fluid by pressure work. By contrast, the physical-chemical and design principles involved in the continuous flow micropumps vary profusely. They include ultrasonic, electrohydrodynamic, electroosmotic, magnetohydrodynamic or electrochemical actuation. These

micropumps do function but require sophisticated fabrication processes and involves complex sealing problems – see the referred reviews for details. Sen *et al.* (1996) proposed a rotating micropump, where the relatively large viscous forces at these small scales are used to drive the fluid.

The viscous micropump combines the simplicity in design with effectiveness in pumping. Roughly speaking, the viscous micropump consists of a cylinder asymmetrically placed inside a micro-channel. The need for the rotor asymmetry can be understood, for instance, by considering an I-shaped micropump with no pressure load across the channel. If the rotor is located at the center of the channel, symmetry leads to zero net flow, regardless of the direction in which the rotor spins. However, if the symmetry is broken and the rotor is placed, say, closer to the top wall, as a clockwise rotor spins a net flow from the right to the left is generated. In this case, the symmetry break provides a preferential direction due to the increase in the shear between the fluid and the upper wall.

After its introduction in 1996, the viscous micropump has been the subject of a stream of publications including Sharatchandra *et al.* (1997), Sharatchandra *et al.* (1998), DeCourtye *et al.* (1998), Abdelgawad *et al.* (2004), Gad-el-Hak (1999), Abdelgawad *et al.* (2005) and da Silva *et al.* (2006). These authors examined various design features and fundamentals issues associated with such micropumps, including the effects of channel height, rotor eccentricity and angular velocity on the pump performance Sen *et al.* (1996), slip velocity Sharatchandra *et al.* (1997), thermal effects Sharatchandra *et al.* (1998), transient effects Abdelgawad *et al.* (2004), multistage configurations Abdelgawad *et al.* (2005) and power consumption and novel geometries da Silva *et al.* (2006). Although extensive and detailed, all previous reports have worked with Newtonian fluids.

In the face of the above, the main objectives of the present work are twofold: to determine the optimal geometrical parameters (i.e., channels thickness and rotor eccentricity) that result in maximum mass flow rate per unit of power shaft consumed, for non-Newtonian fluids, and to introduce and analyze the performance, again for non-Newtonian fluids, of our novel L- and U-shaped micropumps (da Silva *et al.* 2006) when compared with the traditional I-shaped design pioneered by Sen *et al.* (1996). Non-Newtonian fluids abound in Nature – the most notorious example in biomedical applications being blood. A simple non-Newtonian constitutive law is the so-called power-law model that postulates a power-law dependence of viscosity on the strain-rate. This model provides a good approximation of the stress-strain relationship for some biological fluids, including the whole human blood Walburn and Schneck (1976). In the present work we investigate the micro-pump design for blood flow as well as general bio-fluids that can be approximated by the power-law model.

The paper is organized as follows: in §2 we describe the micropump configuration and the numerical modeling. After that, in §3 we validate our numerical results by comparing our present results with the results reported by Sharatchandra *et al.* (1997) and Abdelgawad *et al.* (2004) for Newtonian fluids, and also with an analytical solution for a Non-Newtonian fluid. With the validated model we proceed with the definition of the figure of merit and optimization procedure: in §4 for blood flows and in §5 for general power-law fluids. In the last section §6 we sum up the main findings of this work.

2. Geometrical and Numerical Modeling

Consider the three micropump configurations shown in Fig. 1, where D represents the diameter of the rotor, L_u and L_d are the lengths of the upstream and downstream conduit channels and H is the height of the conduit channel. Due to viscous diffusion, the clockwise-turning rotor impels the fluid from left to right against an imposed pressure difference $\Delta P = P_H - P_L$.

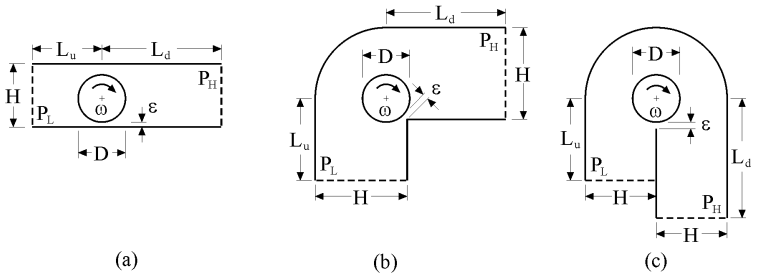

Figure 1. Numerical domain of a viscous micro pump: (a) I-shaped channel, L-shaped channel and U-shaped channel.

Because the effectiveness of a viscous micropump is associated with the eccentricity of the rotor with respect to the surrounding walls, we introduce a linear dimension ε that measures the distance between the lower wall and the rotor (see Fig. 1). For all three configurations, $\varepsilon = 0$ means that the rotor touches the lower wall not allowing any fluid flow between the lower wall and the rotor. If $\varepsilon > 0$, the rotor does not touch the lower wall and fluid is allowed to flow between the rotor and the adjacent surfaces. Finally, $\varepsilon < 0$ means that the rotor is partially embedded in the lower wall. Taking D as our length scale, the dimensionless geometrical parameters can be written as

$$(H, L_u, L_d, \varepsilon)^* = (H, L_u, L_d, \varepsilon)/D \tag{1}$$

The fluid is considered to be non-Newtonian, with a viscosity given by the power-law model

$$\eta = m\,\dot{\gamma}^{n-1} \tag{2}$$

where m and n are the consistency coefficient and the power law index respectively, and $\dot{\gamma}$ is the shear rate, which reads as

$$\dot{\gamma} = \nabla\vec{V} + \nabla\vec{V}^{T} \tag{3}$$

Because of the slow character for the flow, no instabilities are expected and the flow is assumed steady, laminar and incompressible. We define the following dimensionless variables

$$(u, v)^{*} = (u, v)/(\omega\, D/2),\ P^{*} = (P_H - P_L)/[m(\omega\, D/2D)^{n}) \tag{4}$$

and write the dimensionless governing equations as

$$\nabla\cdot\vec{V}^{*} = 0\,, \tag{5}$$

$$\mathrm{Re}_D\,(\vec{V}^{*}\cdot\nabla)\vec{V}^{*} = -\nabla P^{*} + \nabla\cdot\eta[\nabla\vec{V}^{*} + (\nabla\vec{V}^{*})^{T}]\,, \tag{6}$$

where $\mathrm{Re}_D = \rho(\omega\, D/2)^{2-n}\, D^{n}/m$ is the Reynolds number based on the rotor angular velocity and diameter.

Three different micro scale viscous pump configurations were considered: (i) a straight or I-shaped pump, (ii) a L-shaped pump and (iii), a U-shaped pump. The numerical domain is shown directly in Fig. 1 as the area surrounded by the dashed lines at the inlet and outlet, and the solid lines which guide the flow from the inlet to the outlet. The area of the rotor is not accounted for in the numerical simulations.

The flow boundary conditions are: $P^{*} = P_L{}^{*} = 0$ at the inlet and $P^{*} = P_H{}^{*}$ at the exit plane, where $P_H{}^{*} = \Delta P^{*} - P_L{}^{*}$. The pressure boundary condition at the inlet and outlet is implemented as $\mathbf{n}\cdot\mathbf{T} = -P_L$ at the inlet and $\mathbf{n}\cdot\mathbf{T} = -P_H$ at the outlet, where $\mathbf{T} = \sigma\mathbf{n}$ is the stress vector and σ is the Stokes stress tensor $\sigma = -p\mathbf{I} + \nu\,(\nabla\mathbf{u} + \nabla\mathbf{u}^{T})$. In addition, the tangential components of the velocities are set to zero (i.e., $\mathbf{t}\cdot\mathbf{u} = 0$) at the inlet and outlet of the micropump. Non-slip velocity conditions were used in all internal surfaces of the channel. The velocity of the rotor surface is maintained constant at $U = \omega\, D/2$ for each run. We adopted zero tangential velocities at the inlet and outlet after many numerical tests indicated that fully developed flow conditions at the inlet and outlet were obtained for values of L_u and L_d of the order of 4D when n = 1. However, due to the non-linear variation of the moment diffusion given by the power-law relation of Eq. (2), in all numerical simulations starting in Fig. 4, L_u and L_d were set equal to 4D and 12D respectively.

Our numerical simulations were performed using the Finite Elements Method toolbox COMSOL Multiphysics®, v. 3.2 from COMSOL, Inc. Second and first order Lagrange $\mathbf{P_2}$-$\mathbf{P_1}$ mixed finite-elements were used. The mesh density was exhaustively tested in order to guarantee that the results were mesh-independent (the mesh density accuracy test is omitted for brevity). For all three configurations of Fig. 1, the optimal number of elements is between 5000 and 10000 when the objective is to calculate the average flow velocity, which are distributed unevenly through the numerical domain (i.e., a denser mesh is applied to the surroundings of the rotor). When the computation of the group $W'^{*}/\mathrm{Re}_D{}^{2}$ is required, an even higher concentration of elements was used around the rotor, which increases the total number of elements to over 15000 on average, depending on the channel height.

The solution was obtained with a stationary non-linear solver based on a damped Newton's Method. The relative error convergence criterion is the weighted Euclidian norm defined as

$$\mathrm{err} = \left[\frac{1}{N}\sum_{i}\left(\frac{|E_i|}{W_i}\right)^{2}\right]^{1/2} \tag{7}$$

where N is the number of degrees of freedom, $\mathbf{E}_i$ is the estimated error of a current solution vector $\mathbf{U}_i$, defined as: $\mathbf{E}_i = -f(\mathbf{U}_i)/\,f'\,(\mathbf{U}_{i-1})$, and $W_i = \max(|\mathbf{U}_i|, \mathbf{S}_i)$ are the weighted factors. The $\mathbf{S}_i$ factor is defined as the product of a constant, in this case 0.1, times the average of all $|\mathbf{U}_j|$ for all the degrees of freedom named 'j'. The damping factor was set initially equal to 10^{-4} and the convergence criterion was set equal to 10^{-6}.

3. Validation of the Method

The validation of the numerical code started by setting the power-law index equal to the unit (i.e., n = 1) in order to compare the present data against previous results obtained by Sharatchandra *et al.* (1997) and Abdelgawad *et al.* (2004). The comparison evaluated the effect of the channel height on the average fluid velocity ($\bar{u}$) at the exit plane between

the present results and the results obtained by Sharatchandra *et al.* (1997), considering $Re_D = 1$, $\Delta P^*=1$, and $\varepsilon_{mod} = 0.25$, where the average fluid velocity is defined as

$$\bar{u}= H^{-1}\int_0^H u(y)dy, \tag{8}$$

and the modified eccentricity of the rotor (ε_{mod}) is defined as,

$$\varepsilon_{mod} = 0.5(H^* - 1) - \varepsilon^*, \tag{9}$$

where ε^* is the dimensionless eccentricity defined in Eq. (1). A comparison, which is omitted for brevity, shows an acceptable overall agreement between the present results and the results of Sharatchandra *et al.* (1997), where differences smaller than 2% on average is observed.

Figure 2 shows the direct comparison between the average flow velocity data obtained in present study and the results from Sharatchandra *et al.* (1997) and Abdelgawad *et al.* (2004) for an I-shaped viscous micropump versus the group $\varepsilon_{mod}/\varepsilon_{max}$, where ε_{max} represents the design where the rotor is placed at a distance of 0.05 radii from the lower wall. The Reynolds number (Re_D) and the pressure load (ΔP^*) were set equal to the unit. Two values of the channel thickness were considered: $H^* = 1.5$ and 2.5. According to Fig. 2, a nearly prefect agreement between our results and the results of Sharatchandra *et al.* (1997) is obtained throughout the whole of $\varepsilon_{mod}/\varepsilon_{max}$ considered.

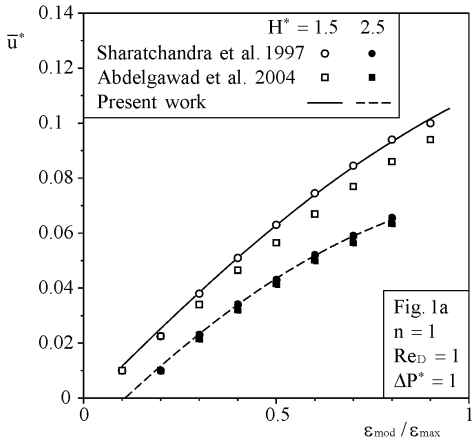

Figure 2. a) Validation of the numerical implementation for a Newtonian fluid.

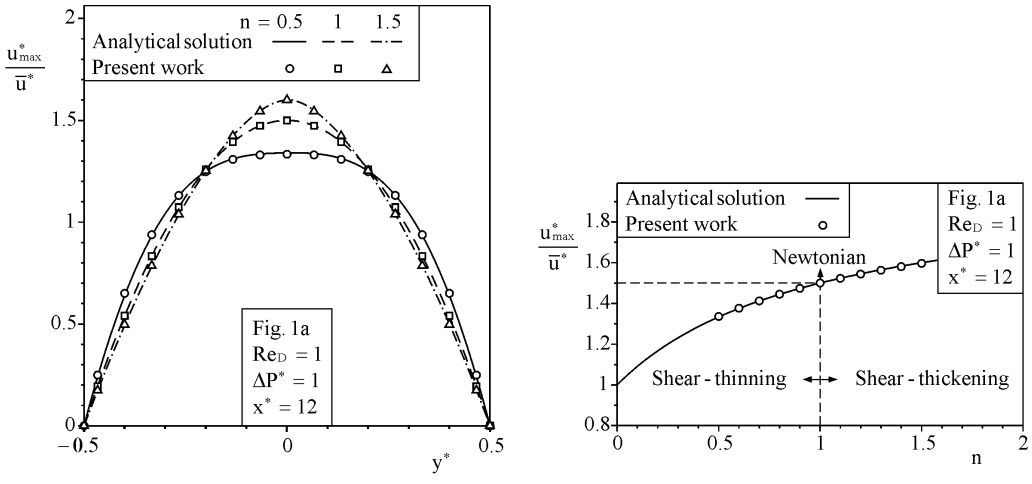

Figure 3. a) Validation of the channel flow fully developed velocity profile for three types of fluids: (a) shear thinning (n = 0.5), (b) Newtonian (n = 1) and (c) shear thickening (n = 1.5). (Left frame)
b) Comparison between the analytical and numerical ratio ($u^*_{max}/\bar{u}^*$) for $0.5 \le n \le 1.5$. (Right frame)

In the next step, Fig. 3a, we compare the effect of the power-law index on the fluid velocity profile for the micro pump shown in Fig.1a. The longitudinal location selected is located at 4D's of the channel exit plane (i.e., $x^* = 12$). The fully developed velocity profile reads as Bird *et al.* (2001)

$$\frac{u}{U_{mean}} = \frac{(1+2n)}{(1+n)}\left[1 - \left(\frac{y^*}{2}\right)^{1+1/n}\right], \tag{10}$$

where y^* indicates the dimensionless distance measured from the center of the channel. Figure 3a shows a perfect agreement between Eq. (10) and the numerical results for three values of n: 0.5, 1 and 1.5, which not only verifies that the flow is fully developed before the end of the channel, but also reinforces the zero tangential components of the velocities at the exit plane (i.e., $(\mathbf{t} \cdot \mathbf{u}) = 0$). Finally, we reach the code validation closure by comparing the ratio $u(y^* = 0)/U_{mean}$ between the numerical results and Eq. (10) for several values of n. Similarly to the comparison presented in Fig. 3a, Fig. 3b depicts a perfect agreement between analytical and numerical solution. One should note that, when n = 1 (i.e., Newtonian fluid), that ratio $u(y^* = 0)/U_{mean}$ returns the well-known value of 3/2 for a fully developed flow between parallel plates.

4. Blood Flow

As previously stated, the present study has two main objectives: (i) to determine the optimal geometrical parameters (i.e., channels thickness H^* and rotor eccentricity ε^*) that result in maximum mass flow rate ($\dot{m}^*$), and (ii), to study the performance of our newly proposed L and U-shaped micropumps when compared with the traditional I-shaped design pioneered by Sen *et al.* (1996) while working with non-Newtonian fluids. The mass flow rate per unit of length is defined as

$$\dot{m}^* = \bar{u}\, H^*. \tag{11}$$

In the first round of optimization (Figs. 4-6), no constraints were considered and the optimal geometric dimensions (i.e., channels thickness H^* and rotor eccentricity ε^*) were determined based on parameters such as Re_D and n. In this scenario, the optimization opportunity emerges from the fact that a micro scale viscous pump operates based on two main conditions: (i) the need of a certain level of confinement (i.e., a finite value for H^*) and (ii), the asymmetric placement of the rotor inside the channel.

The existence of the optimum geometry can be understood by noting that, in the limit of large channel height, the fluid average velocity tends to zero and consequently, the mass flow rate also approaches zero. In the other limit of 'small' values of the dimensionless channel thickness, it is clear that the flow is constricted between the rotor and the upper wall of the pump's channel, which also reduces the mass flow rate. Based on the above, an optimal value for the channel height such that the mass flow rate is maximized must exist; see da Silva *et al.* (2006). Moreover, changing the eccentricity and channel height strongly affects the power consumption of the micropump, leading to an optimum design constrained to power consumption.

4.1 Optimal Design of an I-Shaped micropump

The search for the optimal geometrical configuration started with the simplest design possible, Fig. 1a. The fluid is assumed non-Newtonian with a power-law index of n = 0.785, which according to Walburn and Schnech (1976), presents a good fit for human blood. In this case, we have two degrees of freedom, the channel thickness H^* and the eccentricity ε^*. Assuming fixed values for ε^*, Re_D and ΔP^*, we were able to find an optimal value for the channel height H^* that maximizes the average flow velocity ($\bar{u}$) and the mass flow rate ($\dot{m}^*$) just by varying H^*. Figure 4 shows that the channel thickness has a strong effect on $\bar{u}$ and $\dot{m}^*$, which strengthens the need for optimizing geometric parameters in a viscous micropump. Figure 4 also shows that different values of the optimal channel height (H^*_{opt}) are needed to maximize $\bar{u}$ and $\dot{m}^*$. Also interesting is the differentiated effect of non-optimal channel height on $\bar{u}$ and $\dot{m}^*$. According to Fig. 4, the selection of a channel height smaller than H^*_{opt} is much more detrimental to $\bar{u}$ and $\dot{m}^*$ when compared to a channel height in which $H^* > H^*_{opt}$.

Figure 5a shows the effect of the rotor eccentricity on the mass flow rate and average fluid velocity for an I-shaped pump with the following operating conditions: $Re_D = \Delta P^* = 1$. Each one of the open symbols shown in Fig. 5a represents the maximum value of $\dot{m}^*$ (squares) and $\bar{u}$ (circles) the can be obtained for a given value of ε^*. That is because, implicit in each symbol, is the optimization of $\dot{m}^*$ and $\bar{u}$ with respect to the channel thickness H^*, which is shown later in Fig. 5b. According to Fig. 5a, the maximum values of $\dot{m}^*$ and $\bar{u}$ are found around $\varepsilon^*_{opt} \sim 0$, which represent the maximum mass flow rate and average flow velocity optimized with respect to two degrees of freedom, ε^* and H^*. Furthermore, Fig. 5a also reveals that, differently from Fig. 4, where values of H^* smaller than H^*_{opt} were more detrimental to our two figures of merit (i.e., $\dot{m}^*$ and $\bar{u}$), in Fig. 5a, the eccentricity ε^* also plays a major role on $\dot{m}^*$ when $\varepsilon^* \neq \varepsilon^*_{opt}$, specially if $\varepsilon^* > \varepsilon^*_{opt}$. On the other hand, Fig. 5a shows that it maybe desirable to have $\varepsilon^* < \varepsilon^*_{opt}$ (i.e., the rotor partially embedded in the lower wall) due to the weak effect of the negative eccentricities on the average flow velocity.

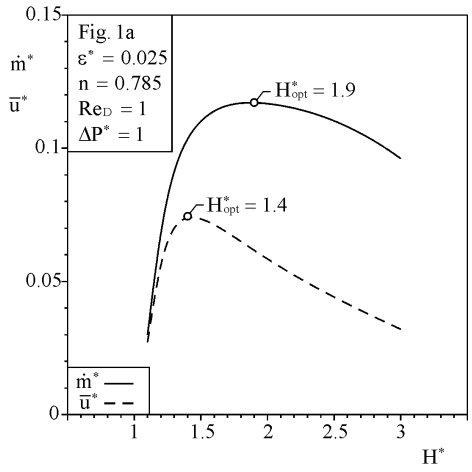

Figure 4. a) Effect of the of the channel height on the average fluid velocity and mass flow rate.

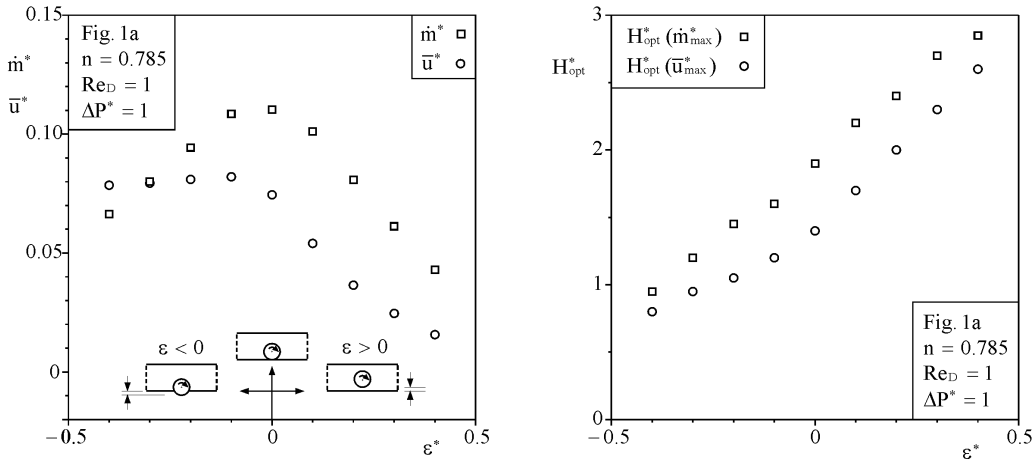

Figure 5. a) Effect of the rotor eccentricity on the maximized average fluid velocity and mass flow rate for the viscous micropumps given in Fig. 1a. (Left frame)
b) Effect of the rotor eccentricity on the optimal channel height for the viscous micropumps. (Right frame)

Figure 5b shows the effect of the eccentricity ε^* on the optimal channel height H^*_{opt}. According to Fig. 5b, H^*_{opt} increases monotonically with ε^*, which can be explained based on the required asymmetric placement of the rotor inside the channel (see §4). This means that any increment in ε^* is associated with an increment in H^*_{opt} so that a certain level of asymmetry can be sustained.

4.2 Curved Housed Micro Pumps

So far, we have demonstrated that significant improvement in terms of mass flow rate can be achieved with the correct selection of the channel height of an I—shaped pump. Next, we attempt to improve the already optimized micropump by aligning the housing of the pump with the rotor. As a results, two new micropump configurations are proposed: and L-shaped pump (Fig. 1b) and a U-shaped pump (Fig. 1c). The performances of the three configurations are presented not only in terms of maximum mass flow rate ($\dot{m}^*_{max}$) and optimal channel height (H^*_{opt}), but also in terms of the shaft power demanded by the rotor (W'^*). The relevance of the shaft power demanded by the rotor originates from the need to compare the performance of microscale pumps on similar basis (i.e., mass flow rate generated per unit of shaft power consumed). We start by defining the rotor's moment coefficient as

$$M = -\int_0^{2\pi} \tau \, d\theta \, . \tag{12}$$

Next, knowing that the torque per unit of length applied to rotor is $T' = M\, 2\pi\, R^2$ and that shaft power per unit of length is $W' = T\, \omega$, one can define the dimensionless shaft power per unit of length applied at the rotor as

$$W'^{*} = \frac{W'}{(m\,V^{n-1}/D^{n-1})^3/(\rho\,D)^2} = M^{*}\,Re_D^2\,. \tag{13}$$

In order to validate our numerical code, a preliminary data obtained for the dimensionless shaft power was compared against the numerical results obtained by Abdelgawada *et al.* (1997) in the steady state limit, since they performed a transient analysis of a Newtonian fluid. One should note that Abdelgawada *et al.* (1997) defined the rotor eccentricity as

$$\varepsilon_{mod,1} = 1 - 2\varepsilon^{*}/(H^{*} - 1)\,. \tag{14}$$

A comparison of the dimensionless shaft power per unit of length applied at the rotor, which is omitted for brevity, shows an acceptable overall agreement between the present results and the results of Sharatchandra *et al.* (1997), where differences smaller than 2% on average is observed.

Figure 6a depicts the effect of the shape of the micropump housing on the maximized figure of merit ($\dot{m}^{*}_{max}$), on the optimal channel height (H^{*}_{opt}) and on the shaft power requirement for a blood–like fluid (i.e., n = 0.785). According to Fig. 6a, the maximized mass flow rate, which is shown by the open bars, increases from left to the right. Furthermore, the shaft power demanded by the rotor decreases in the same direction, which indicates that the overall performance of micropumps (i.e., mass flow rate per unit of shaft power consumed) increases as the shape of housing approaches the shape of rotor. The draw back of micropump with curved housings (e.g., Fig. 1b and 1c) is that they require larger channel heights in order to operate optimally when compared with straight housed pumps (Fig. 1a). This can be observed in Fig. 6a by noticing that H^{*}_{opt} increases from the left (Fig. 1a) to the right (Fig. 1c).

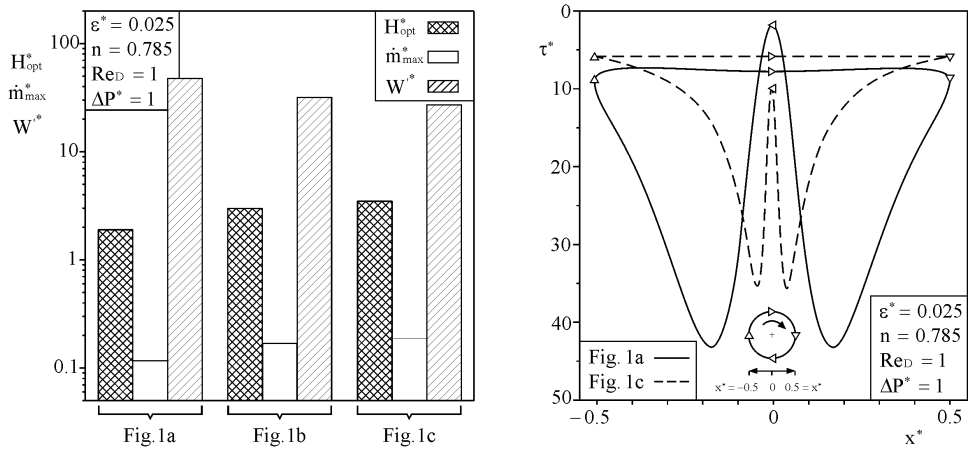

Figure 6. a) Effect of the shape of the micropump on the maximized mass flow rate, optimal channel height and shaft power demanded for a blood-like fluid (Left frame).
b) Effect of the shape of the micropump on the shear distribution over the rotor for a blood-like fluid (Right frame).

Figure 6b shows the shear distribution over the rotor's surface for an I-shaped pump (solid line) and a U-shaped pump (dashed line). One should notice that each one of the two curves is composed by four shear-distribution segments, which are separated by open triangles with different orientations. The triangle orientation coincides with the rotor's surface velocity vector as indicated in the rotor shown in the lower half of the figure. For instance, one can see that the shear distribution on the upper half on the rotor in mostly flat for and U-shaped micropump. Also, because the slow character of the flow, a symmetric shear distribution upstream and downstream can be seem around the rotor's center for both types of micropump. Furthermore, it is important to observe that the integral of the shear around the rotor's surface represents the shaft power required by the rotor divided by Re_D^2. This means that the difference in terms of shaft power demanded shown previously in Fig. 6a between the I-shaped and the U-shaped pumps is mostly due to the reduction of the shear around the lower half of the rotor. It is also note worthy that the alignment of the flow with the rotor provided by the U-shaped housing is also partially responsible for reducing the total required torque required by the rotor, since it brings the shear distribution of the upper half of rotor closer to the zero-shear ordinate when compared with an I-shaped housing as shown in Fig. 6b.

4.3 Optimal Design of U-Shaped Housing

In this section we search for even higher levels of performance of U-shaped pumps by studying the effect of the asymmetric placement of the rotor within micropump housing. As shown in Fig. 7a and 7b, the rotor now is free to

move vertically (ε_v^*) and horizontally (ε_h^*), where ε_v^* and ε_h^* represent respectively the vertical and horizontal distances between the center of the rotor and the center of the housing. These two variables can assume positive or negative values. For instance, Fig. 7a presents a configuration where both vertical and horizontal eccentricities are positive, and in Fig. 7b, both eccentricities are negative. Mixed combinations of positive eccentricities are also permitted. The objective is to analyze the effect of ε_v^* and ε_h^* on the mass flow rate. In order to reduce the number of degrees of freedom, the total channel height in constrained at $H_{tot}^* = 7$, which is twice as large as the optimized height of a U-shaped micropump shown previously in Fig. 6a for the same operating conditions ($Re_D = \Delta P^* = 1$ and $\varepsilon^* = 0.025$), where $\varepsilon_v^* = \varepsilon_h^* = 0$ (i.e., $H_{opt,in}^* = H_{opt,out}^* = H_{tot,opt}^*/2 = 3.5$). The fluid viscosity follow the power-law index suggested by Walburn and Schnech (1976), where n = 0.785.

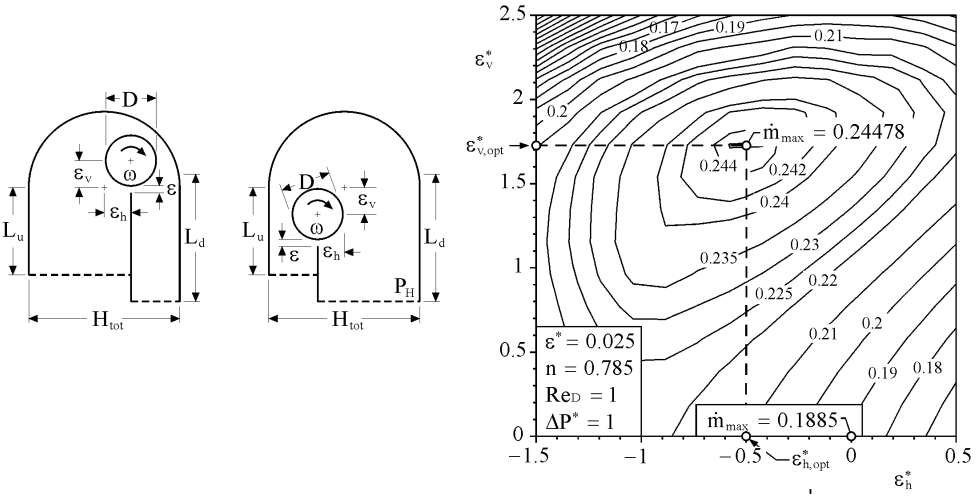

Figure 7. a) U-shaped viscous micropump with an asymmetric rotor, $\varepsilon_h > 0$ and $\varepsilon_v > 0$ (Left frame).
b) U-shaped viscous micropump with an asymmetric rotor, $\varepsilon_h < 0$ and $\varepsilon_v < 0$ (Middle frame).
c) Effect of the vertical and horizontal eccentricity on the mass flow rate (Right frame).

Figure 7c shows a contour plot that has as ε_v^* as ordinate and ε_h^* as abscissa. The curves represent constant mass flow rate designs given by a combination of the two degrees of freedom ε_v^* and ε_h^*. At a location $\varepsilon_v^* = \varepsilon_h^* = 0$, one can observe the maximum mass flow rate offered by a symmetrical configuration. The same value (i.e., $\dot{m}_{max}^* = 0.1885$) can be seen in Fig. 6a. Once ε_v^* and ε_h^* are added as degrees of freedom, the iso-mass flow rate curves show that higher levels of performance can be reached when the rotor is positioned at $\varepsilon_v^* \cong 1.72$ and $\varepsilon_h^* \cong -0.5$. The difference in performance between the two configurations is of the order of 30%. Also interesting is the fact that, because the total channel height is constrained ($H_{opt}^* = 7$), the maximum distance between the rotor's surface and the curved housing of the micropump is 3 dimensionless units, which happens when $\varepsilon_v^* = \varepsilon_h^* = 0$. For instance, if $\varepsilon_h^* = 0$, the rotor will touch the housing when $\varepsilon_v^* = 3$. This explains why the mass flow rate decreases when $|\varepsilon_v^*|$ or $|\varepsilon_h^*| \rightarrow 3.5$, as shown in the upper left corner of Fig. 7c.

5. Effect of the power-law on the optimal design

Figure 8a extrapolates the results presented in Fig. 6a for a wider range of the power law index, $0.5 \le n \le 1.5$. According to Fig. 8a, the trend observed previously in Fig. 6a holds throughout the whole range of the power law index considered. Micro scale viscous pumps with curved housing (i.e., L and U-shaped micropump) perform better (i.e., present higher values of $\dot{m}_{max}^*$) and at the same time, consume less shaft power than the I-shaped pump. As expected, Fig. 8a also shows that the power-law index has a strong effect on the dimensionless shaft power and maximized mass flow rate, since the shear rate is given by Eq. 3. Fluids with larger n have more ability to transfer momentum than a fluid with small n, which explains why $\dot{m}_{max}^*$ increases with n and at the same time why W'^* decreases with n. More important is the fact that the difference between the performances of the micro scale viscous pumps shown is Fig. 1 is sustained throughout the range on n considered proofing the superiority of micro scale pumps with curved housing when compared with an I-shaped pump.

Figure 8b shows the distribution of shear stress over the rotor's surface for a U-shaped pump operating with three different types of fluids (i.e., n = 0.5, 1 and 1.5). The symmetry of the shear distribution is due to the slow character of the flow. More interesting is the effect of the power-law index on the shear distribution. According to Fig. 8b, the overall shape of the shear distribution around the rotor is preserved for different values of the power-law index. However, the whole shear distribution curve, moves towards the zero-ordinate line as n increases. This behavior

explains the decrease in shaft power required by micro scale pumps operating with shear-thickening fluids as shown previously in Fig 8a when compared when pumps operating with shear-thinning fluids.

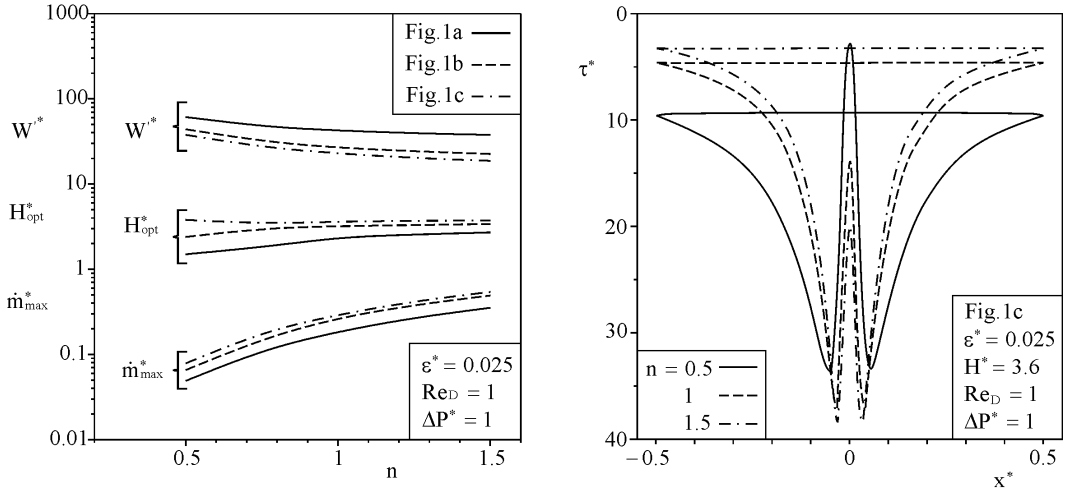

Figure 8. a) Effect of the power-law index on the optimal channel height, maximized mass flow rate and demanded shaft power. (Left frame)
b) Effect of the shape of the power-law index on the shear distribution over the rotor of a U-shaped micropump for a blood-like fluid (n = 0.785). (Right frame)

6. Conclusions

In this paper we presented and evaluated three different configurations of non-Newtonian micro scale viscous pumps for biomedical devices. The objective was to maximize the mass flow rate of a blood-like fluid per unit of shaft power consumed by the rotor, where the fluid shear-rate was given a power-law relation. The optimal geometrical design originated from certain geometrical conditions (§4) required to having an operational micro scale viscous pump. First, the channel housing for the micro scale viscous pump has to provide a certain level of confinement for the rotor. Secondly, the rotor has to be asymmetrically placed inside the channel.

The need for such requirements was verified by a preliminary parametric analysis on an I-shaped micro pump (§4.1), which showed that both conditions are crucial for the pump functionally, and more importantly, the channel height and the rotor eccentricity have a major effect on the mass flow rate. These finding clearly shows the relevance of the geometric optimization of the pump's housing. The numerical simulation also showed that slightly larger values for the optimized channel height (H_{opt}) are expected when the performance of the micro viscous pump is optimized based on the mass flow rate rather than average flow velocity. However, regardless the figure of merit (i.e., mass flow rate or average flow velocity) maximized results are expected as $\varepsilon \to 0$.

Next, in §4.2, two novel configurations of micro viscous pumps with curved housing (Figs. 1b and 1c) were proposed and numerically optimized for maximal mass flow rate while operating with a blood-like type of fluid. The results showed that pump configurations in which surrounding walls the are aligned with the rotor (i.e., Fig. 1b and 1c) provided larger mass flow rates and required less shaft power to operate when compared with straight housed pumps (Fig. 1a). This is an important finding that further supports the use of curved housed micro pumps in mobile or implanted medical devices, which have limited power resources.

In §4.3 we showed that the performance of and U-shaped micro scale viscous pump could be greatly improved by allowing the rotor to move vertically (ε^*_v) as well as horizontally (ε^*_h). More specifically, it was shown that, for a fixed value of the total channel thickness ($H^*_{tot,opt}/2 = 3.5$), the maximized mass flow rate can be increase by 30% if instead of having $\varepsilon^*_h = \varepsilon^*_v = 0$ (concentric configuration), we choose a non-concentric design where $\varepsilon^*_v \cong 1.72$ and $\varepsilon^*_h \cong -0.5$.

The numerical results presented in §5 also showed that, for a power-law index between $0.5 \le n \le 1.5$, micro scale viscous pumps with curved housing provide not only larger mass flow rates, but also require less shaft power when compared with an I-housed micro scale viscous pump.

Acknowledgement
A. K. da Silva thanks the College of Engineering of the University of Hawaii for a 2006 Seed-Grant Award.

Nomenclature

D rotor diameter, m
H channel height, m
L channel length, m

m consistency coefficient, Pa s^n
$\dot{m}$ mass flow rate, kg s^{-1}
M moment coefficient, N m^{-2}
n power-law index
P pressure, Pa
Re_D Reynolds number, ($Re_D = \omega D^2/2\nu$)
T torque, N m
$\bar{u}$ mean velocity, m s^{-1}
$\vec{V}$ velocity vector, m s^{-1}
W' rotor shaft power per unit of length, N s^{-1}

Greek Symbols

γ shear rate, s^{-1}
ε eccentricity, m
η viscosity, kg m^{-1} s^{-1}
ρ density, kg m^{-3}
ω rotor angular velocity, ($\omega = 2U/D$)

Subscripts

d downstream
max maximum
opt optimum
u upstream

Superscript

* dimensionless variables

References

Abdelgawad M, Hassan I, Esmail N. 2004. Transient behavior of the viscous micropump. Microscale Thermophysical Engineering 8:361-381.

Abdelgawad M, Hassan I, Esmail, N, Phutthavong P. 2005. Numerical investigation of multistage viscous micropump configurations. Journal of Fluids Engineering 127:734-742.

Auroux PA, Iossifidis D, Reyes DR, Manz A. 2002. Micro Total Analysis Systems. 2. Analytical standard operations and applications. Analytical Chemistry 74:2637-2652.

Bird RB, Stewart WE, Lightfoot EN. 2001. Transport Phenomena, New York: John Wiley & Sons.

COMSOL MultiPhysics Inc., (2005). User's Manual, Los Angeles, CA 90024.

da Silva AK, Kobayashi MH, Coimbra CFM. 2006. Optimal Theoretical Design of 2D Viscous Micro-Scale Pumps for Maximal Mass Flow Rate and Minimum Power Consumption. International Journal of Heat and Fluid Flow. (in press)

DeCourtye D, Sen M, Gad-el-Hak M. 1998. Analysis of Viscous Micropumps and Microturbines. International Journal of Computational Fluid Dynamics 10:13-25.

Gad-el-Hak M. 1999. The fluids mechanics of microdevices – The Freeman Scholar Lecture. Journal of Fluids Engineering 121:5-33.

Judy JW. 2001 Microelectromechanical systems (MEMS): fabrication, design and applications. Journal of Smart Materials and Structures 10:1115-1134.

Laser DJ, Santiago JG. 2004. A review of micropumps. Journal of Micromechanics and Microengineering 14:R35-R64.

Micci MM, Ketsdever AD. 2000. Micropropulsion for Small Spacecraft. American Institute of Aeronautics and Astronautics Inc. Reston, Va:399 – 422.

Nguyen NT, Huang X, Chuan, TK. 2002. MEMS-Micropumps: a review. Journal of Fluids Engineering 124:384-392.

Reyes DR, Iossifidis D. Auroux PA, Manz A. 2002. Micro Total Analysis Systems. 1. Introduction, theory, and technology. Analytical Chemistry 74:2623-2636.

Sen M, Wajerski D, Gad-el-Hak M. 1996. A novel pump for MEMS applications. Journal of Fluids Engineering 118: 624-627.

Sharatchandra MC, Sen M, Gad-el-Hak M. 1997. Navier-Stokes simulations of a novel viscous pump. Journal of Fluids Engineering 119:372-382.

Sharatchandra MC, Sen M, Gad-el-Hak M. 1998. Thermal aspects of a novel viscous pump. Journal of Heat Transfer 120:99-107.

Verpoorte E. 2002. Microfluidic chips for clinical and forensic analysis, Electrophoresis 23: 677-712.

Walburn FJ, Schneck DJ. 1976. A constitutive equation for the whole human blood, Biorheology 13:201-210.

Woias P. 2004. Micropumps – past, progress and future prospects. Sensors and Actuators B 105:28-38.

Ziaie B, Baldi A, Lei M, Gu Y, Siegel RA. 2004. Hard and soft micromachining for BioMEMS: review of techniques and examples of applications in microfluidics and drug delivery. Advanced Drug Delivery Reviews 56:145-172.